

## Research Article

# Fractal Analysis of Failure Process and Damage Evolution of Jointed Sandstone Based on DIP Technique

ZiQi Liu <sup>1</sup>, LuLin Zheng <sup>1</sup>, Hao Liu <sup>2,3</sup>, Chun Zhu,<sup>4</sup> WenJiBin Sun,<sup>1</sup> XiaoRong Liu,<sup>1</sup> Qing Qiu <sup>1</sup> and ZhiBin Hao<sup>1</sup>

<sup>1</sup>Mining College, Guizhou University, Guiyang, Guizhou 550025, China

<sup>2</sup>Resources and Environment College, Guizhou University, Guiyang, Guizhou, 550025, China

<sup>3</sup>Department of Civil and Environmental Engineering, Technical University of Catalonia (UPC), Barcelona 08034, Spain

<sup>4</sup>School of Earth Sciences and Engineering, Hohai University, Nanjing 210098, China

Correspondence should be addressed to LuLin Zheng; llzheng@gzu.edu.cn

Received 14 March 2022; Accepted 7 April 2022; Published 20 April 2022

Academic Editor: Fuqiang Ren

Copyright © 2022 ZiQi Liu et al. This is an open access article distributed under the Creative Commons Attribution License, which permits unrestricted use, distribution, and reproduction in any medium, provided the original work is properly cited.

The Lannigou gold mine deposit is mainly composed of calcium-bearing sandstone and siltstone, and there are a lot of microdefects such as joints and cracks in the sandstone. The mesostructure of jointed sandstone makes a difference to the fracture process and mechanical properties. The RFPA<sup>2D</sup> software and Digital Image Processing Technology (DIP) were used to create a real microscopic structural numerical model of jointed sandstone with varied dip angle prefabricated cracks. A digital image-based rock microscopic scale fracture box dimension algorithm was established with MATLAB software. It is used to analyze the fractal characteristics of the acoustic emission field of unique prefabricated fractured sandstone. This study demonstrates that the mechanical parameter of jointed sandstone with different prefabricated cracks have manifest anisotropy, which includes elastic modulus and compressive strength. When the leaning angle of the cracks increases, they all increase linearly. There are three modes of starting-crack under uniaxial compression: from the peak of the prefabricated crack; from the middle of the prefabricated crack; and from the joint. Damage degree and rupture model are quantitatively represented by the fractal dimension. The more fractal dimensions there are, the more serious the damage, and the more complicated the rupture mode becomes. This research offers a novel method for investigating the evolution of rock microscopic scale fractures. This has to have engineering practical value for in-depth studies of rock fracture, instability, and failure, as well as the mechanisms that cause rock engineering disasters.

## 1. Introduction

The “Golden Triangle” of Dian, Qian, and Gui is one of China’s Carlin-type gold deposit regions, with over 800 tons of gold resources [1]. Lannigou Gold Mine is the largest deposit in the region [2]. The ore types are mainly calcium-bearing sandstone and siltstone, which has good exploration and exploitation potential. Due to the long-term influence of various geological processes, there are an abundance of joints, fissures, and other microdefects in the sandstone in the mining area. The crack initiation, propagation, and run through in the rock are all part of a dynamic evolutionary process. This process affects the strength and stability of the

rock under the engineering or the environment. It also results in the formation of complex mesostructured sandstone, complicating its mechanical behavior and damage evolution [3, 4]. The rock mass is distributed with fissures of different dips direction and dips, which will have a significantly affected on the fracture damage mechanism of the rock mass [5]. The mesostructure and internal defects of rock are closely related to the macroscopic deformation of the rock mass during the rock failure process. As a result, studying rock deformation and damage evolution from the standpoint of micromechanics is an important and hot topic in the field of rock mechanics today. This has significant scientific significance and engineering practical significance

for in-depth study of rock fracture, instability, and failure and the occurrence mechanism of rock engineering disasters [6].

Many scholars have been making the study of the initiation and propagation of cracks in rocks and have received a lot of research results. Griffith proposed that the stress concentration near the crack tip of a rock mass with an opening type crack was the lead cause of rock mass rupture [7]. Nemat-Nasse et al. used the method of linear elastic fracture mechanics to study the initiation, propagation, and penetration mechanisms of varying amounts and different spatial arrangements of pretensioned cracks. It also reveals the stress concentration phenomenon caused by the interaction between multiple cracks and free surfaces. A related theoretical model was created. The strength of its interaction factors was analyzed [8]. Liu et al. used the Geo-CAAS system to study the deformation and strength characteristics of rocks with single and multiple random defects under uniaxial compression, and the influence of the position and volume content of the defects on the strength of the rock was analyzed [9]. Wong et al. carried out split failure test on a rock sample containing a precrack. He combined numerical simulation to examine the influence of factors such as sample width, preset crack length, and inclination on the crack initiation, propagation, and failure mode [10]. Liu et al. used real-time laser holographic interferometry and other methods to continuously and dynamically observe the crack propagation and failure process of rock samples, and the changes in the mechanical properties of rock cracks are analyzed [11]. Zhao et al. performed uniaxial compression tests on brittle rock-like specimens with precrack. The global strain field evolution process diagram of the sample is obtained by using digital technology [12–14]. In addition, the crack propagation path and stress field distribution characteristics at different stages of the loading process are analyzed. Under uniaxial compression, Li et al. investigated the acoustic emission characteristics and mechanical behavior of fractured coal samples with various dip angles [15].

Above research results have significant reference value for understanding the failure and damage evolution of fractured rock mass in macroscale. However, it rarely involves the uneven distribution of stress and local failure caused by rock microheterogeneity. Because the microscopic heterogeneity of rock determines its macroscopic fracture process, taking into account, the heterogeneity caused by the material's internal structure in the numerical model will help to reveal the rock's fracture mechanism more deeply.

The study used DIP technique to describe the microscopic inhomogeneity of joint sandstone, which is then combined with the RFPA<sup>2D</sup> software to create a real microscopic numerical model that took into account different inclination fractured sandstone. The impact of sandstone mesostructure on the macromechanical properties and mesoscale fracture process of fractured sandstones with different dip angles was investigated. The fractal characteristics of sandstone mesoscale fracture acoustic emission distribution and damage evolution process in numerical experiments are discussed in depth. The research results can not just merely enhance the understanding of mechanism of single crack propagation in rock but also

provide references for the related research of rock damage and fracture.

## 2. Finite Element Method for Crack Growth Simulation

*2.1. Characterization of the Real Mesostructure.* Digital image processing is a new technology of image processing. It entails converting study objects into digital photographs, then analyzing and processing the image information by computer to obtain the required research results. A rectangular matrix of image elements (pixels) constitutes a digital image. Each pixel is an area at which transverse and longitudinal scan lines cross. Each scan line is of equal width, and the brightness, also known as the grayness, of each pixel is represented by an integer. Red (R), green (G), and blue (B), the three basic colors, are comprised in each pixel. Each pixel is made up of R, G, and B functions. As a result, three discrete functions are necessary to mathematically characterize image information in color space. Because it is closely comparable to how humans see color, Hue, Saturation, and Intensity ((brightness) HSI) space is also employed as a substitute for true color space. The predominate wavelength of the color, which is the major color property observed by humans, is represented by the hue component H (with values ranging from 0 to 360). The color purity is represented by the saturation component S (which ranges from 0 to 1). Only the brightness or color brightness is represented by luminance component I (from 0 to 1). This is a more humane way of describing color.

The geometric shape and spatial distribution of the material's mesocomponent are differentiated by digital image processing technologies using gray and color differences. The difference in brightness and color of distinct media in the rock is thresholded using this approach. It can divide each medium's distribution to provide the material's nonuniformity characterization image [16, 17]. Figure 1(a) shows a two-dimensional CT slice acquired from Tianjin Sanying Company's high-resolution CT scanning of a sandstone sample. Found by CT scanning experiment that sandstone mainly contains two kinds of mineral media, named the sandstone matrix and calcite, and the image pixels are 200 pixels  $\times$  500 pixels and the actual size is 40 mm  $\times$  100 mm, and it is a 24 bit color image in BMP format. The color change of the image is not obvious. Thus, image processing to stretch contrast in order to increase the tonal differentiation between the features was conducted using multithreshold segmentation by assessing the fluctuation in values of Intensity (I) in the HIS color space. Figure 1(a) shows the AA' scan line passing through the mineral medium, and Figure 1(b) shows the sandstone surface scan curve. The I value of sandstone is below 150, and the I value of calcite fluctuates is above 150. After a series of observations and experiments, the study settles on I = 150 as the image splitting threshold. Figure 1(c) is the result of performing threshold segmentation on the image of Figure 1(a), where green represents joints (calcite) and dark blue represents sandstone. The spatial distribution and shape of calcite in the sandstone can be seen more precisely using

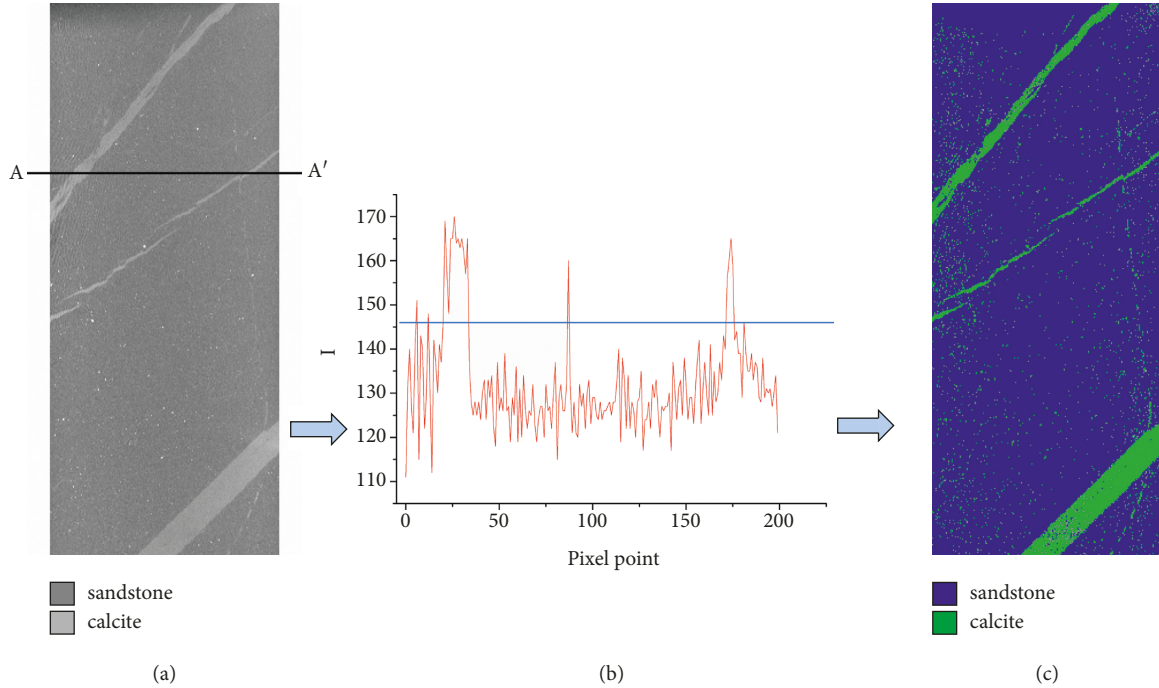


FIGURE 1: Digital image characterization of jointed sandstone. (a) Two-dimensional CT slice. (b) Variation in the I value along scan line AA'. (c) Threshold-segmentation characterization image of sandstone.

the characterization imagery derived through threshold segmentation.

**2.2. The Damage Constitutive Relation on the Mesoscale.** The change of elastic modulus of strain equivalence hypothesis defines the damage variable in RFPA<sup>2D</sup>. When a material is damaged by an external force, the damage constitutive relationship can be described as [18, 19]

$$E = (1 - \omega)E_0, \quad (1)$$

where  $E_0$  is the undamaged material's elastic modulus,  $E$  is the damaged material's elastic modulus, and  $\omega$  is the damage variable.

Because the sandstone's tensile strength is much lower than its compressive strength, we used the maximum tensile stress and Mohr–Coulomb failure/shear strength as element failure criteria, and Figure 2 shows the mesodamage constitutive relationship. There is no damage at first because the stress-strain curve is linearly elastic. Brittle damage occurs when the maximum tensile strain is attained in the meso-element. The principal failure mode of brittle rocks is tensile-induced failure. When the tensile stress reaches the element's tensile strength ( $f_t$ ), damage occurs according to the main damage criteria. The tensile damage function is written as follows [20]:

$$F^-(\sigma) = \sigma_3 + f_t = 0, \quad (2)$$

where the primary stress vector is  $\sigma$ . Under uniaxial tension, the mesoscopic element's constitutive relationship is illustrated in the third quadrant of Figure 2, and can be expressed as follows [21]:

$$\omega = \begin{cases} 0, & \varepsilon_{t0} \leq \varepsilon < 0, \\ 1 - \frac{\lambda \varepsilon t_0}{\varepsilon}, & \varepsilon_{tl} \leq \varepsilon < 0, \\ 1, & \varepsilon \leq \varepsilon_{tl}, \end{cases} \quad (3)$$

where  $\lambda$  denotes the element's residual intensity coefficient, which is defined as  $f_{tr} = \lambda f_t$  (where  $f_t$  is the mesoscopic element's tensile strength and  $f_{tr}$  is the residual strength at the element's initial tensile failure), and  $\varepsilon_{tl}$  is the element's ultimate tensile strain. The element approaches the state of tensile fracture when its uniaxial tensile strain reaches the ultimate tensile strain, and  $\eta$  is the ultimate strain coefficient, which is formally specified as  $\varepsilon_{tl} = \eta \varepsilon t_0$ .  $\varepsilon t_0$  is the tensile strain associated with the elastic limit, also known as the tensile failure strain threshold, and it is calculated as follows [22]:

$$\varepsilon_{t0} = \frac{-f_t}{E_0}. \quad (4)$$

The Mohr–Coulomb criterion is employed as the second failure criterion for mesoscopic elements under uniaxial compression conditions, as seen in the first quadrant of Figure 2, depicting damage to elements under compression or shear stress [23]:

$$F^+(\sigma) = \sigma_1 - \sigma_3 \frac{1 + \sin \phi}{1 - \sin \phi} - f_c = 0, \quad (5)$$

where  $\phi$  represents the friction angle,  $\sigma_1$  and  $\sigma_3$  represent the primary stresses, and  $f_c$  represents the uniaxial compressive

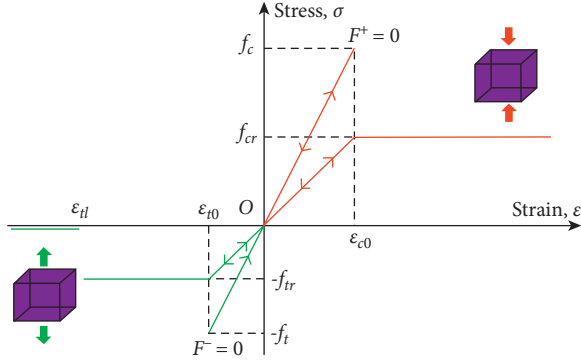


FIGURE 2: Constitutive Relation for mesoelement damage.

strength. Under uniaxial compression, the damage variable  $\omega$  of element can be represented as follows [24, 25]:

$$\omega = \begin{cases} 0, & \varepsilon < \varepsilon_{c0}, \\ 1 - \frac{\lambda \varepsilon_{c0}}{\varepsilon}, & \varepsilon \geq \varepsilon_{c0}, \end{cases} \quad (6)$$

where  $\lambda$  represents the residual strength coefficient, defined as  $f_{tr}/f_t = f_{cr}/f_c = \lambda$ , and  $\varepsilon_{t0}$  represents the compressive strain at the elastic limit, which can be calculated as [24, 25]:

$$\varepsilon_{c0} = \frac{f_c}{E_0}. \quad (7)$$

**2.3. Establishment of Numerical Simulation.** The mesoscopic fracture process of jointed sandstone was simulated using RFPA2D software and digital image processing technology (see Section 2.1 of this article) in this work. Through two-dimensional FEM, RFPA<sup>2D</sup> can model the mesoscopic failure mechanism of rock [16, 17, 22–25], and Section 2.2 shows the constitutive model of damage to the element. The actual size of this experimental model is 40 mm × 100 mm. The image is divided into 200 × 500 and 100,000 pixels, and the whole characterization image is transformed into 100,000 finite element meshes. Each finite element grid can characterize different mesoscopic materials in the sandstone sample (see Figure 3). The higher the brightness, the greater the elastic modulus. According to the characterized color and brightness, each material component is assigned a parameter value and the material parameters of each microscopic medium are shown in Table 1 [26]. This model analyses the inhomogeneity of sandstone and calcite, while the mechanical parameters of the mesoelements are assigned using the Monte-Carlo technique [27, 28].

To investigate the differences in mechanical characteristics of jointed sandstones with varying inclination angles cracks, as well as the impact of sandstone mesoscopic heterogeneity on the evolution of macrofracture damage. To ensure that the image's underlying medium remains unchanged, this experiment created seven groups of cracks with varying dip angles ( $\alpha = 0^\circ, 15^\circ, 30^\circ, 45^\circ, 60^\circ, 75^\circ, 90^\circ$ ).  $\alpha$  is the angle formed by the horizontal direction and the fissure

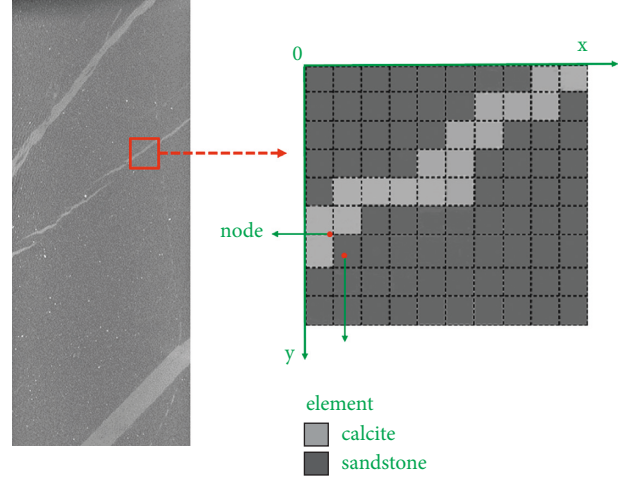


FIGURE 3: Mesh of finite element microscopic of rock samples.

that has been prefabricated (Figure 4). The prefabricated crack is 14 mm long and 1 mm wide, which is contained in the middle of the jointed sandstone (Figure 4). Figure 5 is a simplified diagram of the numerical model loading. The plane strain analysis is used to simulate. The numerical model utilizes axial displacement loading, with the initial displacement set to 0.001 mm, the single-step displacement increment set to 0.0005 mm, and the loading stopping when the specimen is failure. It is presumed that the elastic modulus and strength of sandstone and calcite mesoscale elements obey the Weibull random distribution [29]:

$$f(u) = \frac{m}{u_0} \left( \frac{u}{u_0} \right)^{m-1} \exp \left( -\frac{u}{u_0} \right)^m, \quad (8)$$

where  $u_0$  denotes the average of the mesoelement parameters;  $u$  represents the properties of the mesoelements, such as elastic modulus or strength;  $m$  represents the homogeneity of material, the greater the homogeneity  $m$ , the more uniform the material.

### 3. Results and Discussion

**3.1. Sandstone Mechanical under Uniaxial Compression.** The distribution of primary stress and elastic modulus during the initial stage of loading when  $\alpha = 45^\circ$  is shown in Figure 6. The brighter the figure, the greater the stress. Through comparison, it is found that the stress distribution in the microstructure of sandstone is uneven. At the tip of the prefabricated fracture and the crucial surface (relatively low mechanical surface) of the calcite vein and sandstone, the stress concentration distribution is more visible. This demonstrates that the presence of internal cracks in sandstone, as well as the heterogeneity of the mesostructure, has a significant impact on stress distribution.

The elastic modulus and compressive strength simulation results of seven sets of fractures with varied dip angles in jointed sandstone are shown in Table 2. The elastic modulus and compressive strength of numerical samples varied significantly, as demonstrated in Figure 7, with increasing crack inclination, the specimen's compressive strength

TABLE 1: Material mechanical parameters of jointed sandstone.

Material	Elastic modulus (GPa)	Compressive strength (MPa)	Poisson ratio	Compression-tension ratio	Internal friction angle (C°)
Sandstone	108.2	118	0.16	14	35
Calcite	80.5	101	0.303	11	30

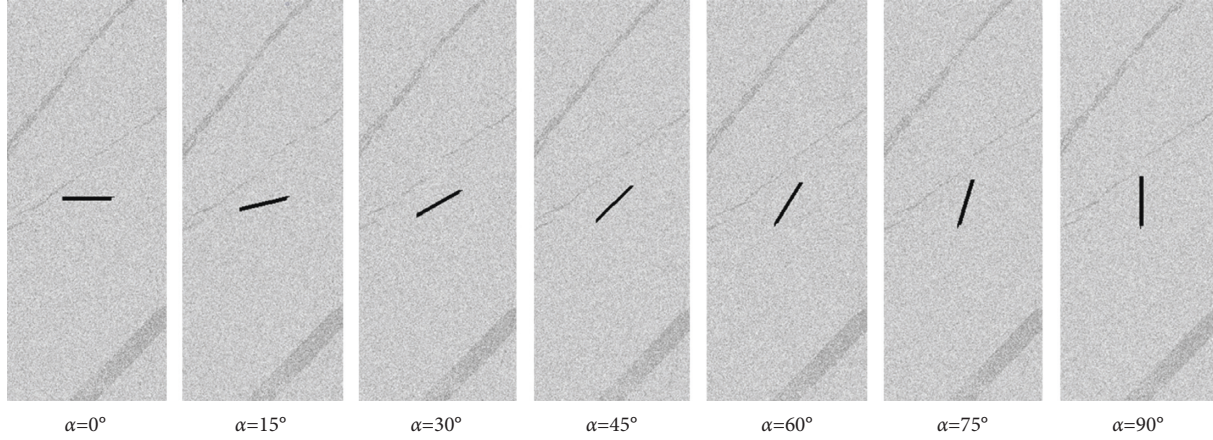


FIGURE 4: Internal fissures in jointed sandstone with various dip angles.

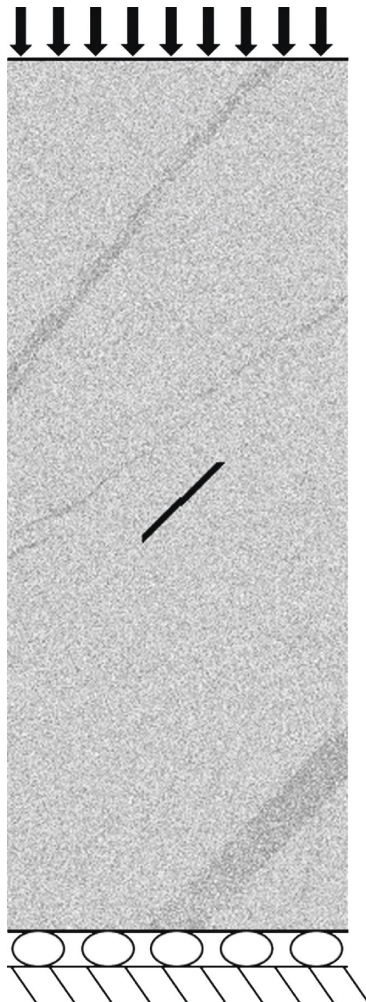


FIGURE 5: A schematic illustration of the numerical model's mechanical loading model.

increases linearly. This is owing to the sandstone's weak calcite cementation, which generates significant anisotropy in its compressive strength. The numerical simulation results are consistent with the research conclusions of Li et al. [15], indicating that the numerical simulation results obtained in this study are reliable. Sandstone's compressive strength peaks at 64.32 MPa when the angle is 90°; it reaches the minimum when the angle is 0°, which is 32.27 MPa, and the difference between the minimum and maximum is 32.05 MPa. The specimen's elastic modulus grows linearly as the crack inclination angle increases. The elastic modulus reaches the maximum value at  $\alpha = 90^\circ$ , which is 107.74 GPa; it reaches the minimum value at  $\alpha = 0^\circ$ , which is 82.49 GPa, with a difference of 25.25 GPa between the minimum and maximum value.

3.2. *Fracture Evolution Process Analysis.* Figure 8 depicts the progression of the numerical sample's acoustic emission and elastic modulus during the fracture process. The color green denotes a compression-shear failure in the present loading step element. The red indicates the tensile failure, and the black indicates the complete failure. When  $\alpha = 0^\circ$ , the cracks began to sprout, extended perpendicular to the center of the prefabricated fractures, and eventually penetrated, as seen in Figure 8. Tensile stress causes wing cracks to form and spread, as seen in the AE diagram, and ultimately resulted in axial splitting failure. When  $\alpha = 15^\circ$ , the wing crack is located about  $\frac{1}{4}$  of the distance from the tip of the prefabricated crack. And the secondary wing cracks that have formed around the lower-end wing crack are all propagating along the weak surface. Tensile stress initiates and propagates wing cracks, which dominate the macroscopic secondary wing cracks on the specimen's weak surface at the right lower corner. As the load increases, upper secondary wing cracks

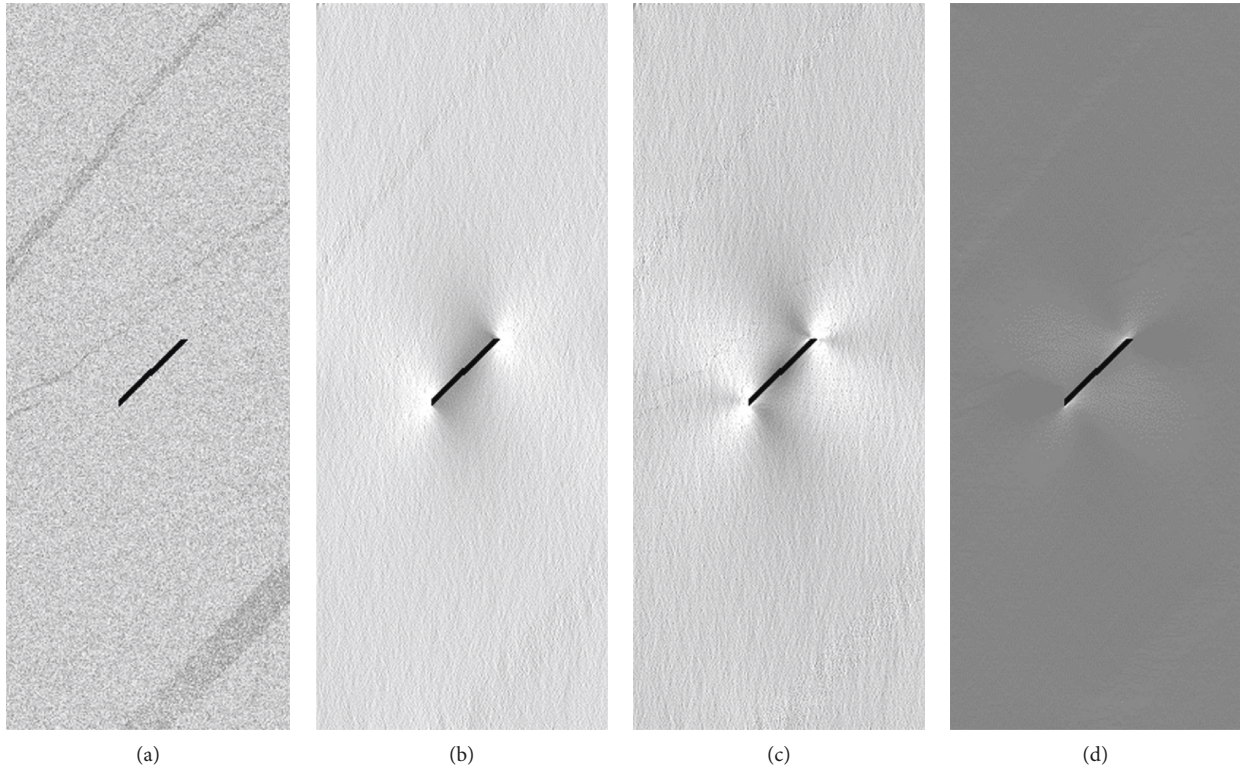


FIGURE 6: Elastic modulus and internal principal stress distribution in sandstone during the initial loading stage. (a) Elastic modulus; (b) max principal; (c) maximum shear stress; (d) minimum principal stress.

TABLE 2: Results of numerical sample simulations for compressive strength and elastic modulus.

Crack dip angle (°)	Compressive strength (MPa)	Elastic modulus (GPa)
$\alpha = 0^\circ$	32.27	82.49
$\alpha = 15^\circ$	35.01	87.20
$\alpha = 30^\circ$	40.33	93.54
$\alpha = 45^\circ$	42.71	98.62
$\alpha = 60^\circ$	49.75	101.34
$\alpha = 75^\circ$	56.30	103.23
$\alpha = 90^\circ$	64.32	107.74

begin to crack, and the wing cracks near the tips of the prefabricated cracks eventually spread the joints in a straight line. Moreover, the upper end near the wing cracks and the cementation point (weak surface) of the sandstone produce shear failure and cause funnel-shaped damage between joints and cracks. The generation of macroscopic shear zones in sandstone was associated with the accumulation of tensile failure elements, as seen in Figure 8(b), and the fractures finally penetrated. When  $\alpha = 30^\circ$  and  $\alpha = 45^\circ$ , the wing crack starts at the tip of the prefabricated crack and propagates along the direction perpendicular to the tip of the prefabricated crack. The crack development trend of the two models in the early stage was similar. However, with the increase of load, a wing crack was initiated near the weak surface of the lower right part of the prefabricated crack at  $\alpha = 45^\circ$ . Due to the hindrance action of the internal

sandstone matrix, the crack did not continue to expand. Instead, the macro secondary wing crack was suddenly initiated at the upper left part of the crack tip. Because tensile stress is constantly acting at the tip of the wing crack, the final specimens will undergo shear failure along the wing cracks and joint ends. In the later stage, the secondary wing cracks will penetrate the specimen, causing it to split axially. When  $\alpha = 60^\circ$ , the wing cracks begin to fracture along the prefabricated crack's tip and expand in the direction of the maximum primary stress. With the increase of load, multiple intermittent secondary cracks are initiated in the opposite direction of the wing crack that has already expanded in the lower part of the prefabricated crack. Furthermore, a macroscopic shear zone is also generated, causing the crack to penetrate. When  $\alpha = 75^\circ$ , the propagation path of the wing crack at both ends of the fracture is similar, but the crack propagation at the lower part is faster. With the increase of load, the lower left part begins to rupture in patches, meantime the upper part breaks in shear. When  $\alpha = 90^\circ$ , cracks initiated at the upper and lower joints of the specimen, and the prefabricated crack tip did not produce a significant mechanical response, which is different from the research of Li et al. [15]. In the study by Li et al. [15], the crack started along the tip of the prefabricated crack and caused the final penetration to produce axial splitting failure. Because this study considered the microscopic uniformity of the rock, the crack along the weak surface initiation and expansion occurs at the place, which eventually leads to splitting and failure of the sample.

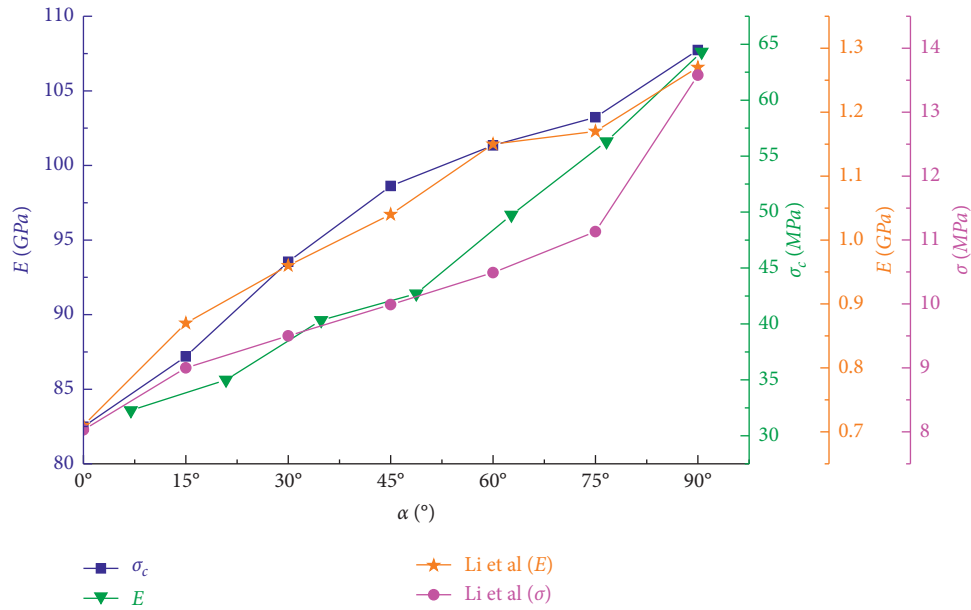


FIGURE 7: Numerical model compressive strength and elastic modulus.

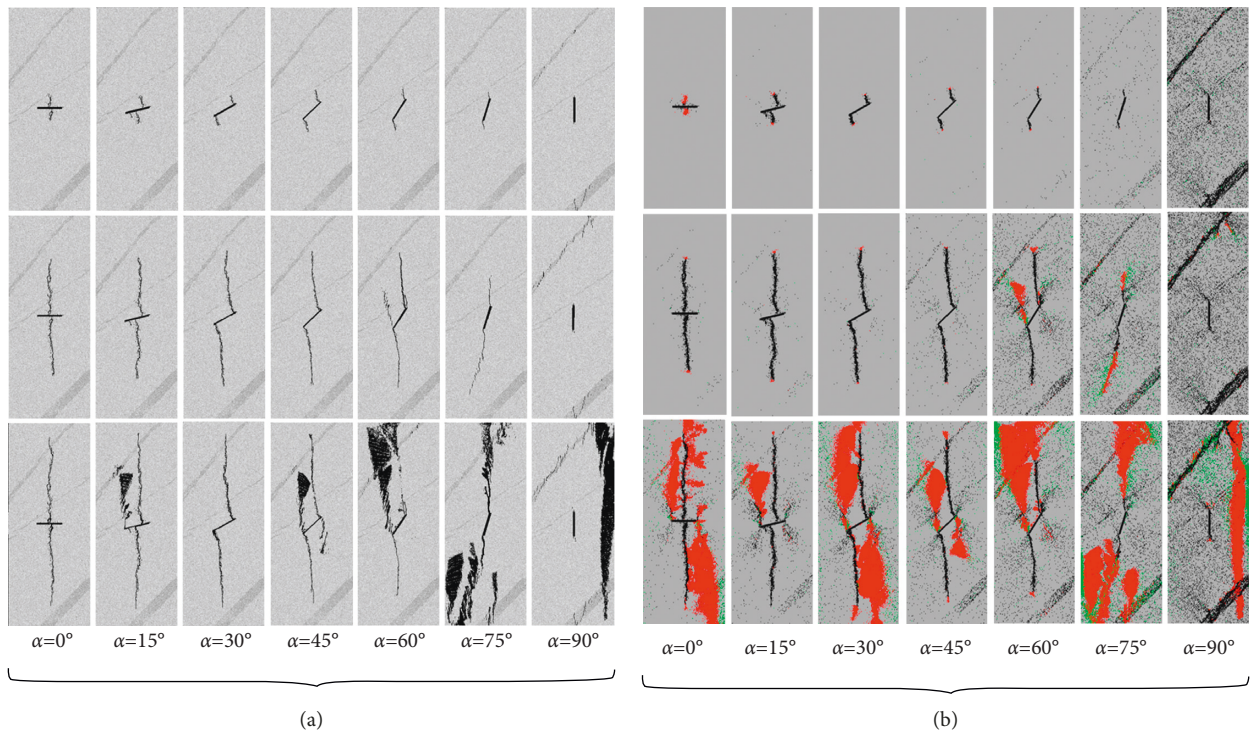


FIGURE 8: The fracture process' acoustic emission development and elastic modulus diagram. (a) Elastic modulus evolution diagram of sandstone fracture process; (b) AE evolution diagram of sandstone fracture process.

3.3. Analysis on the Evolution Characteristics of Acoustic Emission Distribution. Acoustic emission (AE) is a transient elastic wave caused by the quick release of sound source energy as microcracks in the rock form and expand. Every microscopic fracture will produce acoustic emission phenomenon, and it is a measurable response of rock deformation under load, as a result, it is a useful tool for studying how rock's interior damage develops [30]. The failure of each

element is regarded to be the source of an acoustic event in RFPA<sup>2D</sup>. RFPA<sup>2D</sup> can be utilized to model acoustic emission activities because the rock discharges its stored elastic energy all through the fracture process [16–18]. As the rock fracture process can be characterized by the acoustic emission evolution, the damage progression characteristics of the rock can be investigated in depth by measuring the number of damaged elements and the released energy. The relationship

among the AE energy, stress, and accumulated AE energy of the specimen under different loading conditions with the loading step is shown in Figure 9.

The load-step number and acoustic emission-step number curve of the specimen is related to its failure mode. At the initial stage of loading, since there is no element damage, the accumulated AE energy and the AE count are both 0. The stress increases linearly when the loading step is increased. There is a visible stress reduction after peak strength, yet there is still residual strength.

There are two situations in which the process takes place: The rupture modes of  $\alpha = 0^\circ$  and  $\alpha = 30^\circ$  are roughly the same. When the load is located in the elastic stage, the AE signal has appeared. At the same time, element damage occurs inside the sample, and a small sharp increase in AE occurs successively. As the load increases, dense microcracks and acoustic emission signals appear in the sample. When the load reaches the peak stress, the microcracks extend and expand, and the cumulative AE increases roughly exponentially. After the peak stress, stress enters the falling stage, and the microcracks in the sample rapidly expand until they penetrate. There are still many acoustic emission events, and the sample is not completely destroyed. There was no acoustic emission signal in the other samples at the beginning of loading. With the load is continuously applied, when the stress approaches its maximal value, the AE count rises sharply and reaches its maximum. At this time, the crack extends rapidly, the internal crack of the sample penetrates, and the sample is completely destroyed. After the peak, there is still a slight surge in acoustic emission. When  $\alpha = 90^\circ$ , the sample penetrates instantaneously at the peak stress, and the internal damage is the most severe (Figure 9(g)).

**3.4. Fractal Characteristics.** Fractal damage theory is proposed by [31]. Fractal theory can assist and explain the failure mechanism of rock masses by quantitatively describing complex objects in nature [31–35]. Xie and Sun study shows that the whole process of rock from crack initiation to final failure has fractal characteristics [36]. Because the box dimension with self-similarity is simple to compute, we used it to characterize the failure evolution of rocks in the study, which is described as [31, 37]

$$D_s = \lim_{k \rightarrow \infty} \frac{\lg N r_k(A)}{\lg 1/r_k}, \quad (9)$$

where  $D_s$  is the rock damage area's fractal dimension,  $r_k$  is the generated shrinking sequence with the square box size of the element, and the number of grids required to cover the target set  $A$  with a square box of size  $r_k$  with the minimum number of grids is  $N r_k(A)$ .

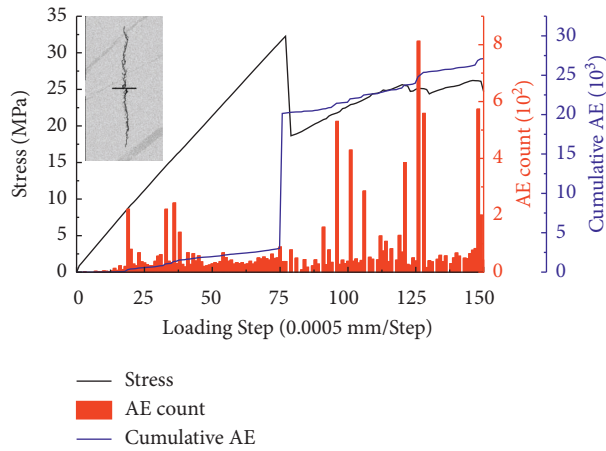
This study is based on the MATLAB platform, using the self-developed digital image and data analysis system of pores and fractures [17] to analyze the acoustic emission graphs at various dip angles and stress levels (as shown in Figure 10). The fractal dimension fitting curve of the rock damage area is shown in Figure 11, the correlation coefficient  $R^2 = 0.9730$ , and the fractal dimension  $D_s = 1.153$ . This

demonstrates that the microscopic scale fracture distribution of sandstone has good self-similarity, and the fractal dimension is very convincing. Table 3 shows the calculation results of fractal dimension and acoustic emission energy of numerical samples under different stress levels.

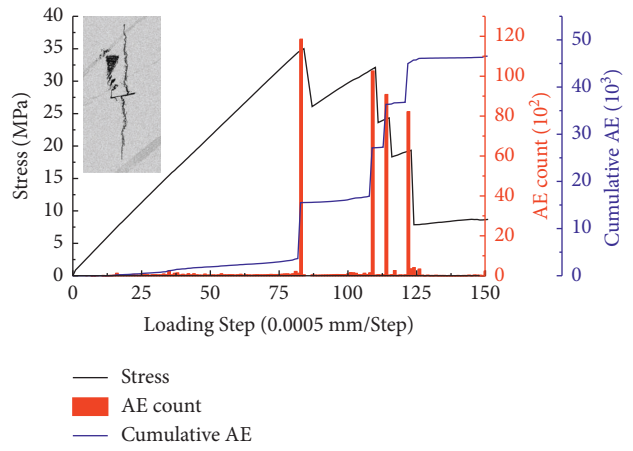
Figure 12 depicts the link between AE energy and various levels of stress. Furthermore, if the stress level is less than 60%, the AE energy curve's amplitude in each set of azimuth angles is quite gentle, and change tends to follow a consistent pattern. When the stress level is greater than 70%, the sample's AE energy curve rapidly rises and maxima at  $\alpha = 90^\circ$ , followed by the sample, when  $\alpha = 75^\circ$  and  $\alpha = 60^\circ$ . As a result, when  $\alpha = 90^\circ$ , the energy produced by the sandstone sample's fracture is the highest, internal damage is the most severe, and ultimate damage is the most serious.

As seen in Figures 13 and 14, with increasing stress levels at all azimuth angles, the fractal dimension continues to increase. The fractal dimension and the load of the rock damage zone have a positive association. In addition, the rise in fractal dimension is timed to coincide with the change in damage. Figure 14 describes and confirms the influence of the prefabricated crack inclination on damage degree of jointed sandstone from a fractal perspective. When the stress level is 10%,  $D_s = 0$ , and the sandstone sample is in the linear elastic stage, indicating that the sample has not been damaged. When the stress level is less than 20%, the  $D_s$  of the samples will rapidly increase. As the stress increases and the  $D_s$  of each sample increases linearly when the stress level is above 30%. Finally, the  $D_s$  value of  $\alpha = 90^\circ$  is 1.86 when the stress level is 100%, which is the crest value. The  $D_s$  value of  $\alpha = 0^\circ$  is 1.41, which is the least value. Analyzing Figures 9 and 12, it concludes that the final rupture mode of the sample is the most complicated when  $\alpha = 90^\circ$ . Besides, it releases the most energy (Figure 12), the internal damage is the most severe, and the ultimate damage is the most serious, so the  $D_s$  is the largest. At  $\alpha = 0^\circ$ , the crack is perpendicular to the middle part of the prefabricated crack and starts to crack and transfixion, the final fracture mode is the simplest with the least energy released (as shown in Figure 12) and the least damage, so the fractal dimension is the smallest. For other samples with prefabricated cracks, the fractal dimension is between  $\alpha = 90^\circ$  and  $\alpha = 0^\circ$ . As a result, the bigger the  $D_s$ , the more severe, the sample damage is, and the more complex, the eventual failure mode is.

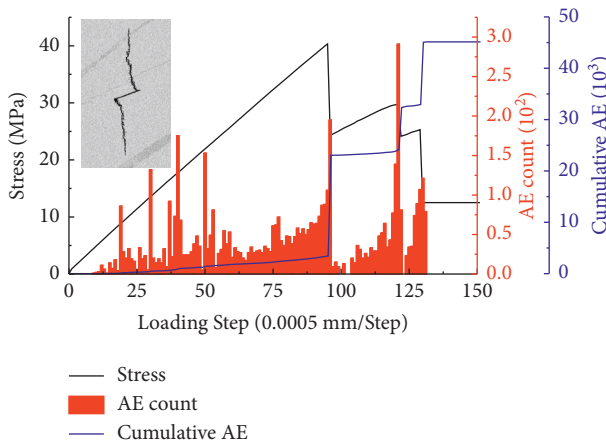
In summary, the fractal research results show rock mesoscale failure evolution process is fractal, and the damage degree of rock failure can be characterized by fractal dimension. Thus, using the box dimension to the rock fracture process analysis based on the acoustic emission field is very effective, the presented method does not take into account a large number of rock mechanics parameters, making it a simple and effective new method for evaluating mesoscale rock damage evolution. Therefore, we may use the method presented in the study to calculate the fractal dimension and evaluate the damage characteristics of rock mesoscale failure, so as to reveal the understanding of the mechanism of rock crack propagation.



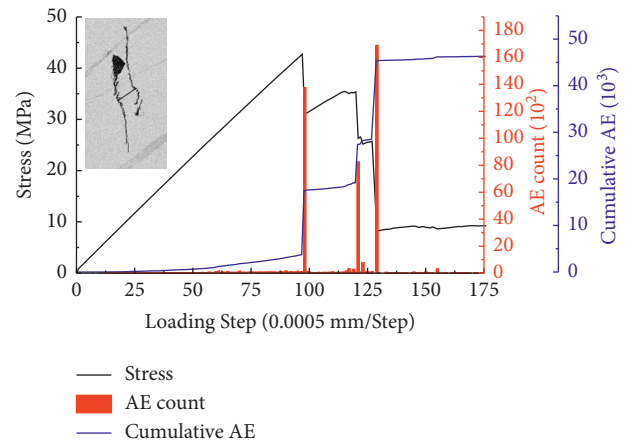
(a)



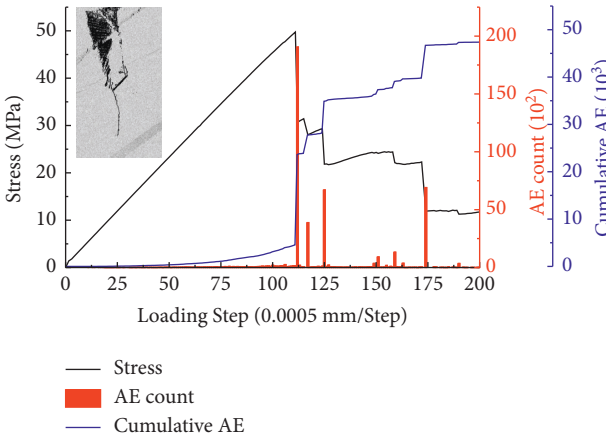
(b)



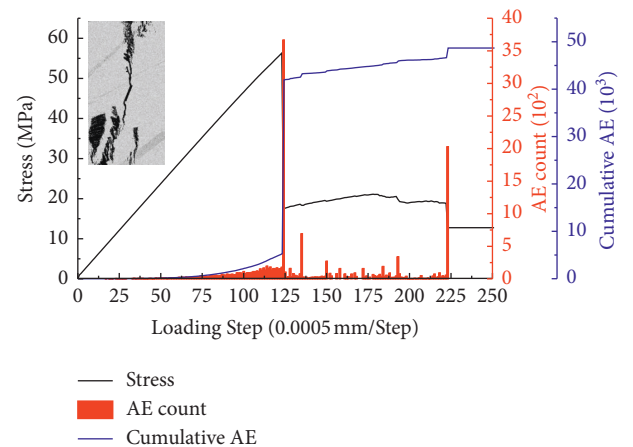
(c)



(d)

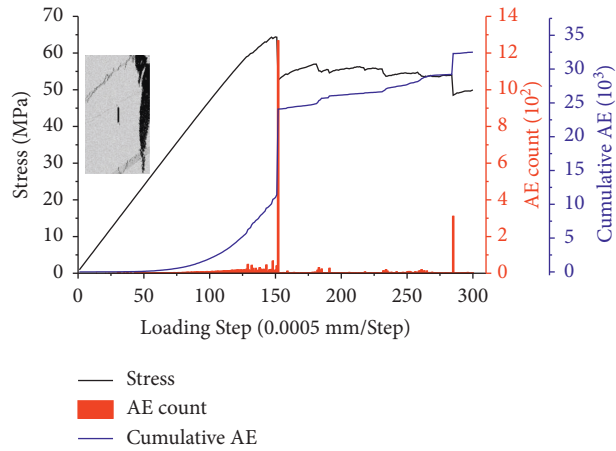


(e)



(f)

FIGURE 9: Continued.



(g)

FIGURE 9: The relationship between the AE energy, stress, and accumulated AE energy of the specimen. (a–g) Specimens 0°, 15°, 30°, 45°, 60°, 75°, 90°, respectively.

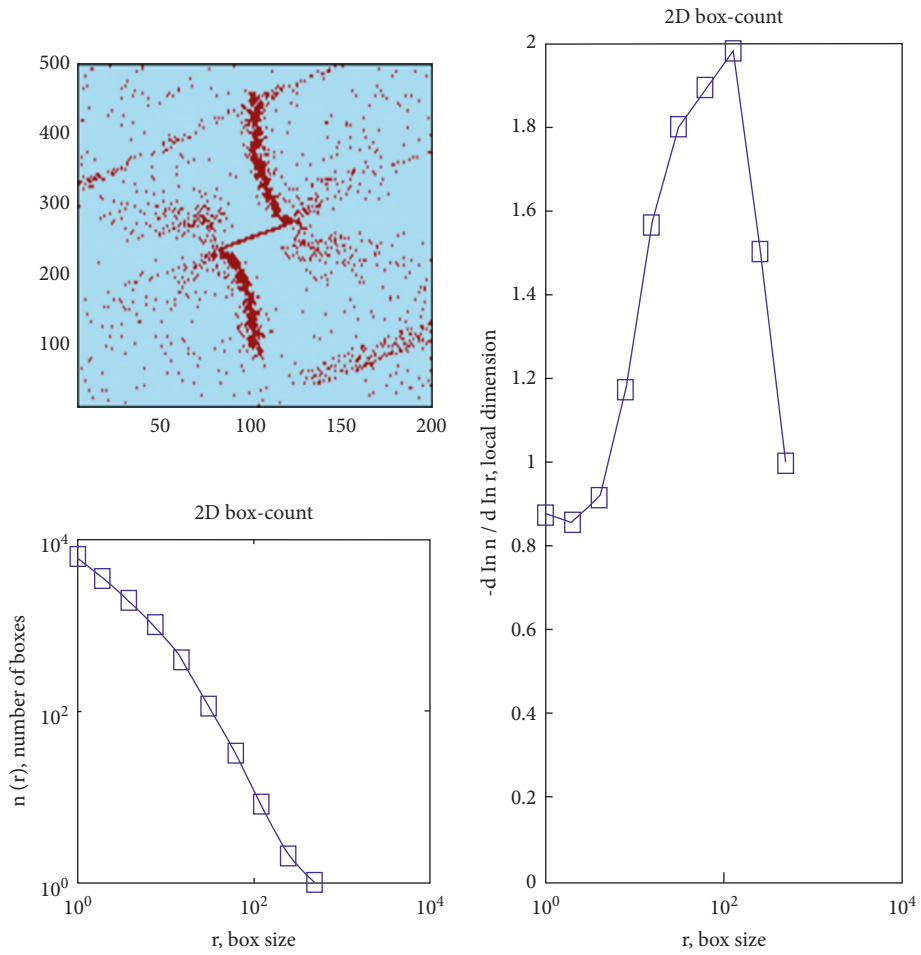


FIGURE 10: Fractal dimension calculation process based on MATLAB ( $\alpha = 45^\circ$ , and stress level is 60%).

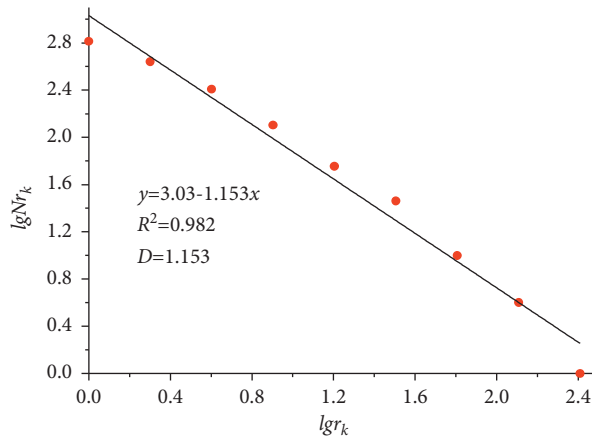


FIGURE 11: Fractal Dimension fitting curve ( $\alpha = 45^\circ$ , and stress level is 60%).

TABLE 3: Calculation results of AE energy and fractal dimension of specimens under different stress levels.

Numerical sample		Stress level									
		10%	20%	30%	40%	50%	60%	70%	80%	90%	100%
$\alpha = 0^\circ$	AE	0	1	18	22	33	65	73	78	82	102
	Ds	0.92	0.88	1.05	1.10	1.20	1.26	1.29	1.36	1.37	1.41
$\alpha = 15^\circ$	AE	0	7	28	42	63	71	86	91	98	116
	Ds	0.84	0.88	1.02	1.09	1.19	1.27	1.31	1.35	1.39	1.47
$\alpha = 30^\circ$	AE	0	18	19	24	38	55	67	88	92	106
	Ds	0.83	0.90	1.04	1.12	1.18	1.24	1.28	1.34	1.39	1.45
$\alpha = 45^\circ$	AE	0	7	18	34	49	66	71	80	95	102
	Ds	0.83	0.86	0.92	0.96	1.06	1.153	1.27	1.35	1.42	1.48
$\alpha = 60^\circ$	AE	0	5	9	11	14	30	32	72	96	149
	Ds	0	0.54	0.95	1.14	1.24	1.31	1.40	1.64	1.76	1.70
$\alpha = 75^\circ$	AE	0	5	7	12	16	33	51	92	112	177
	Ds	0.85	0.82	0.86	0.93	1.05	1.20	1.34	1.41	1.50	1.59
$\alpha = 90^\circ$	AE	0	2	5	10	24	44	58	114	154	193
	Ds	0.87	0.84	0.89	0.99	1.13	1.27	1.40	1.50	1.60	1.86

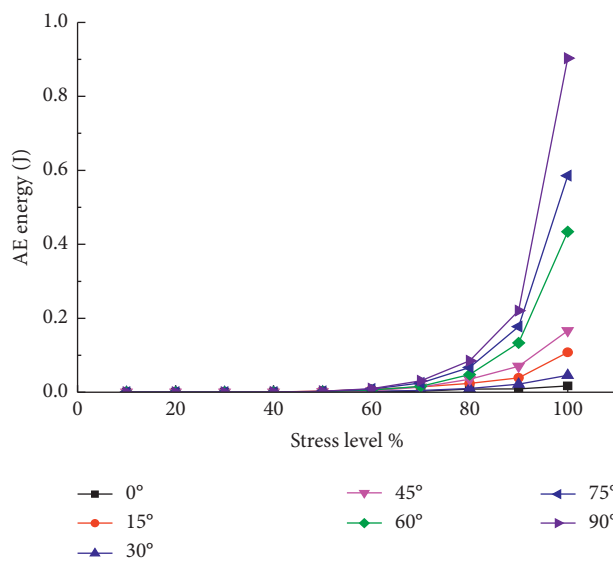


FIGURE 12: Relationship between stress level and AE energy at various azimuths.

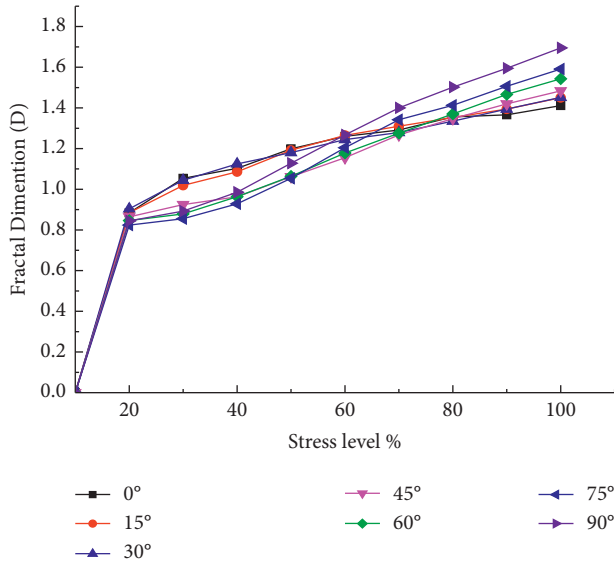


FIGURE 13: Relationship between stress level and fractal dimension at various azimuths.

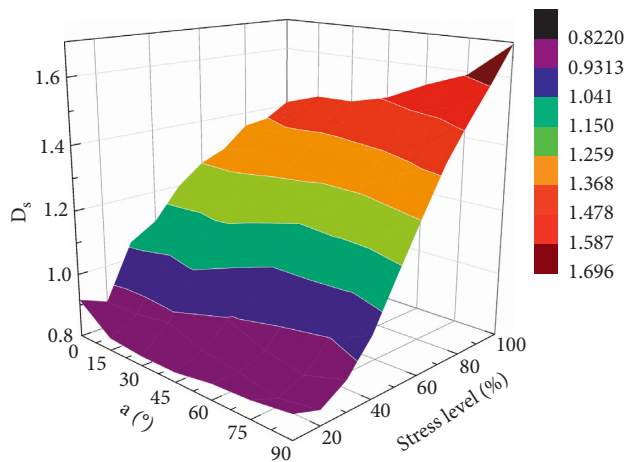


FIGURE 14: Relationship between azimuth, stress level, and fractal dimension.

#### 4. Conclusion

To systematically explore the mesoscopic damage evolution mechanism of jointed sandstone, DIP, micro-CT scanning, and numerical simulation experiments were used. Using DIP and RFPA<sup>2D</sup> software, a numerical model based on real meso-structure is created to investigate the fractal behavior of meso-scale failure in sandstone, and the model is applied to characterize the damage evolution, crack propagation, and failure mode of rock fracture. The following are the primary conclusions:

- (1) Anisotropy is seen in the elastic modulus and compressive strength of jointed sandstone with varied prefabricated cracks. As the inclination of the crack increases, they all change linearly. There are three types of final cracking modes of the sample under uniaxial compression: from the tip of the

prefabricated crack ( $\alpha = 15^\circ$ ,  $\alpha = 30^\circ$ ,  $\alpha = 45^\circ$ ,  $\alpha = 60^\circ$ ,  $\alpha = 75^\circ$ ); from the middle of the prefabricated crack initiation of cracks ( $\alpha = 0^\circ$ ); cracks from the joints ( $\alpha = 90^\circ$ ).

- (2) A digital image-based rock microscopic scale fracture box dimension algorithm was written with MATLAB software. It can quantitatively evaluate the damage evolution process of jointed sandstone with different prefabricated fractures. The conclusion is that as the fractal dimension gets larger, the crack propagation gets more fully, and the rock damage degree gets higher.
- (3) In this study, the  $D_s$  value of  $\alpha = 90^\circ$  is 1.86, and the failure mode is the most complicated. The  $D_s$  value of  $\alpha = 0^\circ$  is 1.41, and the fracture mode is the simplest. Fractal dimension of other prefabricated fracture angle specimens is between these two values. The fractal dimension can be efficiently used to characterize the samples' final failure mode. The bigger the  $D_s$ , the more severe the sample damage is, and the more complex the eventual failure mode is.
- (4) In a further stage of the research, a three-dimensional numerical model of the true microstructure of sandstone with various prefabricated cracks will be created, and its macroscopic failure and mesoscopic evolution mechanisms will be thoroughly investigated.

#### Data Availability

Research data may be obtained by appropriate request.

#### Conflicts of Interest

The authors declare that they have no conflicts of interest.

#### Acknowledgments

This study was funded by the Guizhou Province Science and Technology Support Program Project (no. QIANKEHE Support [2021] General 516) and National Natural Science Foundation of China (nos. 51574093, 41962008, and 51774101).

#### References

- [1] M. H. Chen, J. W. Mao, F. P. Bierlein, T. Norman, and P. J. Uttley, "Structural features and metallogenesis of the carlin-type Lannigou gold deposit, Guizhou province, China," *Ore Geology Reviews*, vol. 43, no. 1, pp. 217–234, 2011.
- [2] M. H. Chen, L. L. Wu, P. J. Uttley, T. Norman, Z. Jianmin, and Q. Yunzhong, "REE features of arseuian pyrite and vein quartz and their fluid inclusions in the Jinfeng (Lannigou) gold deposit, Guizhou province, China," *Acta Petrologica Sinica*, vol. 23, no. 10, pp. 2423–2433, 2007.
- [3] M. L. Huang, "Research on fracture mechanism by interaction of multi-crack in brittle rock," *Chinese Journal of Rock Mechanics and Engineering*, vol. 20, no. 3, p. 423, 2001.
- [4] C. Zhu, M. Karakus, M. C. He et al., "Volumetric deformation and damage evolution of Tibet interbedded skarn under multistage constant-amplitude-cyclic loading," *International*

- Journal of Rock Mechanics and Mining Sciences*, vol. 152, Article ID 105066, 2022.
- [5] Y. T. Du, Y. C. Li, S. L. Zhang, and L. X. Lü, "Propagation mechanism of 3D through fracture with different dip angles under uniaxial compression load," *Journal of Shandong University of Science and Technology*, vol. 35, no. 3, pp. 53–60, 2016.
  - [6] Y. S. Pan, *Study on Rock Burst Initiation and Failure Propagation*, PhD Thesis Tsinghua University, Beijing, China, 1999.
  - [7] A. Griffith, "The phenomena of rupture and flow in solids," *Philosophical Transactions of the Royal Society of London - Series A: Containing Papers of a Mathematical or Physical Character*, vol. 221, no. 582-593, pp. 163–198, 1921.
  - [8] S. Nemat-Nasser and M. Obata, "A microcrack model of dilatancy in brittle materials," *Journal of Applied Mechanics*, vol. 55, no. 1, pp. 24–35, 1988.
  - [9] X. L. Liu, S. J. Wang, E. Z. Wang, J. Wang, and B. Hu, "Evolutionary rules of flaws in rock subjected to uniaxial compression and rock strength," *Chinese Journal of Rock Mechanics and Engineering*, vol. 27, no. 6, pp. 1195–1201, 2008.
  - [10] R. H. C. Wong, P. Lin, and C. A. Tang, "Experimental and numerical study on splitting failure of brittle solids containing single pore under uniaxial compression," *Mechanics of Materials*, vol. 38, no. 1, pp. 142–159, 2006.
  - [11] D. M. Liu, M. F. Cai, Y. B. Zhou, and Z. Y. Chen, "Dynamic monitoring on developing process of rock cracks," *Chinese Journal of Rock Mechanics and Engineering*, vol. 25, no. 3, pp. 467–472, 2006.
  - [12] C. Zhao, C. Bao, H. Matsuda, C. F. Zhao, and J. S. Tian, "Application of digital image correlation method in experimental research on crack propagation of brittle rock," *Chinese Journal of Geotechnical Engineering*, vol. 37, no. 5, pp. 944–951, 2015.
  - [13] C. Zhao, C. Bao, J. S. Tian, H. Matsuda, and C. Morita, "Experimental study of coalescence mode of cracks and strength of rock with double flaws based on strain localization," *Chinese Journal of Rock Mechanics and Engineering*, vol. 34, no. 11, pp. 2309–2318, 2015.
  - [14] C. Zhao, J. S. Tian, and H. Matsuda, "Study on the crack propagation and damage evolution characteristics of rock based on the global strain field under uniaxial compression," *Chinese Journal of Rock Mechanics and Engineering*, vol. 34, no. 4, pp. 763–769, 2015.
  - [15] D. Li, E. Wang, X. Kong, M. Ali, and D. Wang, "Mechanical behaviors and acoustic emission fractal characteristics of coal specimens with a pre-existing flaw of various inclinations under uniaxial compression," *International Journal of Rock Mechanics and Mining Sciences*, vol. 116, pp. 38–51, 2019.
  - [16] Z. Li, L. Li, B. Huang et al., "Numerical investigation on the propagation behavior of hydraulic fractures in shale reservoir based on the DIP technique," *Journal of Petroleum Science and Engineering*, vol. 154, pp. 302–314, 2017.
  - [17] H. Liu, Y. Zuo, Z. Wu, and W. Sun, "Fractal analysis of mesoscale failure evolution and microstructure characterization for sandstone using DIP, SEM-EDS, and micro-CT," *International Journal of Geomechanics*, vol. 21, no. 9, Article ID 04021153, 2021.
  - [18] C. A. Tang, L. G. Tham, S. H. Wang, H. Liu, and W. H. Li, "A numerical study of the influence of heterogeneity on the strength characterization of rock under uniaxial tension," *Mechanics of Materials*, vol. 39, no. 4, pp. 326–339, 2006.
  - [19] Y.-J. Zuo, Q. Zhang, T. Xu, Z.-H. Liu, Y.-Q. Qiu, and W.-C. Zhu, "Numerical tests on failure process of rock particle under impact loading," *Shock and Vibration*, vol. 2015, Article ID 678573, 12 pages, 2015.
  - [20] G. Li and C.-A. Tang, "A statistical meso-damage mechanical method for modeling trans-scale progressive failure process of rock," *International Journal of Rock Mechanics and Mining Sciences*, vol. 74, pp. 133–150, 2015.
  - [21] W. C. Zhu, J. Liu, C. A. Tang, X. D. Zhao, and B. H. Brady, "Simulation of progressive fracturing processes around underground excavations under biaxial compression," *Tunnelling and Underground Space Technology*, vol. 20, no. 3, pp. 231–247, 2004.
  - [22] C. Tang, "Numerical simulation of progressive rock failure and associated seismicity," *International Journal of Rock Mechanics and Mining Sciences*, vol. 34, no. 2, pp. 249–261, 1997.
  - [23] S. Y. Wang, S. W. Sloan, D. Sheng, and C. Tang, "Numerical analysis of the failure process around a circular opening in rock," *Computers and Geotechnics*, vol. 39, pp. 8–16, 2011.
  - [24] S. Y. Wang, S. W. Sloan, C. A. Tang, and W. C. Zhu, "Numerical simulation of the failure mechanism of circular tunnels in transversely isotropic rock masses," *Tunnelling and Underground Space Technology*, vol. 32, pp. 231–244, 2012.
  - [25] L. Zheng, H. Liu, Y. Zuo et al., "Fractal study on the failure evolution of concrete material with single flaw based on DIP technique," *Advances in Materials Science and Engineering*, vol. 2022, Article ID 6077187, 15 pages, 2022.
  - [26] H. Diao, "Rock mechanical properties and brittleness evaluation of shale reservoir," *Acta Petrologica Sinica*, vol. 29, pp. 3300–3306, 2013.
  - [27] R. Y. Rubinstein and D. P. Kroese, *Simulation and the Monte Carlo Method*, John Wiley & Sons, Hoboken, NY, United States of America, 2011.
  - [28] F. Rossi, A. Di Carlo, and P. Lugli, "Microscopic theory of quantum-transport phenomena in mesoscopic systems: a Monte Carlo approach," *Physical Review Letters*, vol. 80, no. 15, pp. 3348–3351, 1998.
  - [29] W. Weibull, "A statistical distribution function of wide applicability," *Journal of Applied Mechanics*, vol. 18, no. 3, pp. 293–297, 1951.
  - [30] Z.-j. Wu, Z.-y. Wang, L.-f. Fan, L. Weng, and Q.-s. Liu, "Micro-failure process and failure mechanism of brittle rock under uniaxial compression using continuous real-time wave velocity measurement," *Journal of Central South University*, vol. 28, no. 2, pp. 556–571, 2021.
  - [31] B. B. Mandelbrot, *The Fractal Geometry of Nature*, W. H. Freeman, New York, 1982.
  - [32] P. Bouboulis, L. Dalla, and V. Drakopoulos, "Construction of recurrent bivariate fractal interpolation surfaces and computation of their box-counting dimension," *Journal of Approximation Theory*, vol. 141, no. 2, pp. 99–117, 2006.
  - [33] H. Liu, L. Zheng, Y. Zuo et al., "Study on mesoscopic damage evolution characteristics of single joint sandstone based on micro-CT image and fractal theory," *Shock and Vibration*, vol. 2021, Article ID 6547028, 18 pages, 2021.
  - [34] B. Liu and Y. Ning, "Application of fractal theory to geotechnical engineering," *Applied Mechanics and Materials*, vol. 52-54, pp. 1291–1295, 2011.

- [35] Q. Wang, M. He, S. Li et al., "Comparative study of model tests on automatically formed roadway and gob-side entry driving in deep coal mines," *International Journal of Mining Science and Technology*, vol. 31, no. 4, pp. 591–601, 2021.
- [36] H. P. Xie and H. Q. Sun, "The foundation of fractal mathematics and the application of fractal in rock mechanics," *Mining World*, vol. 0, no. 4, pp. 1–6, 1996.
- [37] J. Li, Q. Du, and C. Sun, "An improved box-counting method for image fractal dimension estimation," *Pattern Recognition*, vol. 42, no. 11, pp. 2460–2469, 2009.